



Sun, R., & Hallett, S. (2017). Barely visible impact damage in scaled composite laminates: Experiments and numerical simulations. *International Journal of Impact Engineering*, 109, 178-195.
<https://doi.org/10.1016/j.ijimpeng.2017.06.008>

Peer reviewed version

License (if available):
CC BY-NC-ND

Link to published version (if available):
[10.1016/j.ijimpeng.2017.06.008](https://doi.org/10.1016/j.ijimpeng.2017.06.008)

[Link to publication record in Explore Bristol Research](#)
PDF-document

This is the author accepted manuscript (AAM). The final published version (version of record) is available online via Elsevier at <http://www.sciencedirect.com/science/article/pii/S0734743X16306728>. Please refer to any applicable terms of use of the publisher.

University of Bristol - Explore Bristol Research

General rights

This document is made available in accordance with publisher policies. Please cite only the published version using the reference above. Full terms of use are available:
<http://www.bristol.ac.uk/red/research-policy/pure/user-guides/ebr-terms/>

Barely Visible Impact Damage in Scaled Composite Laminates: Experiments and Numerical Simulations

X C. Sun* S R. Hallett

University of Bristol, Queen's Building, University Walk, Bristol BS8 1TR, UK

Ric.sun@bristol.ac.uk (X.C. Sun)

Stephen.hallett@bristol.ac.uk (S R. Hallett)

Abstract

This paper investigates the effect of size and complexity of composite structures on the formation of low-velocity impact damage via experimental tests and numerical modelling. The ASTM standard low-velocity impact test and a scaled-up version of the test were conducted. A novel numerical technique is presented that combines 3D solid and thin 2D shell elements for modelling different domains to achieve a high level of fidelity locally under the impact location, whilst achieving good computational efficiency for large structures. Together with the experimental studies at the different scales, the predictive capability of the numerical models was systematically validated. This modelling method demonstrated an advanced computational efficiency without compromising predictive accuracy. The models are applied to a case study of low-velocity impact of a large-scale stringer-stiffened panel, showing this modelling approach to be suitable for predicating low-velocity impact damage and structural response of laminated composites over a range of sizes and complexities.

Keywords: laminated composites, low-velocity impact, finite element analysis, large complex structure

*Corresponding author: ric.sun@bristol.ac.uk (Xiaochuan Sun); +44(0) 117 33 15311

1. Introduction

Polymer matrix composite materials are being widely and increasingly used in aerospace structures. Despite their superior properties, such as high specific stiffness and strength, over conventional metal alloys, they are susceptible to low-velocity impact, especially for laminated carbon fibre epoxy composites. Different to isotropic materials, laminated composites under transverse loadings easily result in Barely Visible Impact Damage (BVID), the extent of which is not clearly visible from the surface but causes debilitating internal damage. BVID can be caused by runway debris during aircraft take-off and landing or by dropped tools during manufacturing. If the impact velocity is as low as the case of the latter scenario, impact damage is usually dominated by the resin or matrix properties, without the fibre failure. Matrix cracking occurs as the first damage mode at intra-ply locations due to intralaminar shear and tension and acts as a precursor to delamination. Usually driven by interlaminar shear, delaminations occur between plies and are prone to propagate under in-plane compressive loading, which could eventually lead to catastrophic failure of the structure. Delamination is therefore one of the most critical factors limiting design. As laminated composites are used in structures at various locations, the impact damage mechanisms and extent of which, in relation to different size and complexity of the boundary conditions of the structures, is not able to be accurately quantified through the commonly used standard small-coupon experiments (e.g. ASTM-D7136, Boeing BSS-7260, Airbus AITM-1.0010, etc.). It is important to understand the low-velocity impact damage behaviour of composites under the different boundary conditions resulting from such structural applications. This is largely approached by expensive testing regimes, but accurate high-fidelity numerical modelling has a role to play in understanding the various scales and complexities, which could significantly reduce cost and time [1].

Numerous studies in the literature have focused on modelling standard impact events and predicting impact damage using Finite Element Analysis (FEA). By combining Continuum

Damage Mechanics (CDM) at the ply level and Cohesive Zone Modelling (CZM) at interlaminar regions, the degradation behaviour of plies and delaminations induced by low-velocity impact of laminated composites can be captured [2–11]. Adopting CZM only at both intra- and interlaminar levels are also often found in the literature, especially for modelling the interactions between matrix cracks and delaminations of laminated composite under tension, open-hole tension, notched tension and transverse loading [12–20], where damage and degradation within the plies is modelled by cohesive elements placed along the fibre directions, instead of using CDM approach. The full CZM method has been applied to previous studies of laminated composite under static indentation [14,21] and is here implemented further in a dynamic impact environment to investigate the robustness of the modelling approaches developed thus far and extend it to large scale structures.

Numerical models with implementation of either CDM or CZM require considerable computational cost for cases where the laminates have complex stacking sequences and when the dynamic effects are not negligible. The high computational cost and long run times make such FEA models less attractive for impact damage analysis for large and complex composite structures. With the difference in numerical efficiency between 3D solid and thin shell elements for modelling composites, finite element techniques combining different element types in different regions of a composite structure become one of the obvious solutions. In cases such as laminates under point loading or with a geometric discontinuity like a pre-crack, the potential damage locations can be approximated or derived from small-coupon tests in advance, allowing regions with and without damage to be modelled separately, with different element types, in order to reduce cost without losing basic accuracy. Even with a single element type, different mesh schemes at different regions lead to significant improvement in efficiency. Riccio et al. [22,23] and Caputo et al. [24,25] used solid elements throughout in a model to capture the low-velocity impact damage of laminated composite; contact was used to tie the fine-mesh detailed

local domain and coarse mesh global domain. This application was later developed for predicting impact damage in an all-composite wing-box structure [26], and numerical predictions coincided well with experimental data. Approaches, involving solid-shell coupling techniques or similar, have been investigated by numerous researchers for various applications; for example, a mesh superposition technique developed by Gigliotti and Pinho [27], Sellitto et al. [28,29] for a non-matched mesh coupling techniques, Ledentsov et al. [30] for applications of sheet metal forming simulation, Krueger et al.[31–34] in studying composite structures with delaminations, Cho and Kim [35] in investigating bifurcation buckling behaviour of delaminated composites, and Davila and Johnson [36] in predicting compressive strength of dropped-ply laminates. Both computational efficiency and accurate prediction were demonstrated by these studies. Few of the studies in the literature have systematically investigated the effectiveness of global-local modelling approaches for low-velocity impact with fully solid (i.e. accurate but computational heavy) models, combined with experiment results as the structural dimensions and complexity increases.

A high-fidelity numerical modelling strategy, first developed and validated in a previous study on quasi-static indentation [14], is here applied to the case of low-velocity impact. To evaluate the scalability of such modelling techniques for various sizes and boundary conditions of composite structures, impact tests were performed on laminates with two in-plane sizes (i.e. the standard ASTM-D7136 size [26] and a scaled up version of this test). In order to model the larger scale a mesh coupling technique is introduced to combine the accuracy of the solid based high fidelity models, with the structural and computational efficiency of shell elements. This modelling technique was then further applied to a stringer stiffened skin panel as a full structural application example.

2. Specimen Preparation and Experiments

Low velocity impact (LVI) tests were designed and then carried out using an Instron Dynatup 9250 HV drop-weight impact tower. During impact testing, the impact force and displacement were measured by a single accelerometer inside the tup, and the measured data is automatically processed by a 4 kHz filter of the console software to reduce the noise and oscillations. All laminates tested in this work were manufactured from Hexcel's IM7/8552 unidirectional carbon fibre pre-preg sheet and fabricated by hand lay-up and autoclave. Two laminate stacking sequences were used; single-ply laminates with a $[45^\circ/0^\circ/90^\circ/-45^\circ]_{4s}$ layup and blocked-ply laminates with a $[45^\circ_2/0^\circ_2/90^\circ_2/-45^\circ_2]_{2s}$ layup. These are designated as Sublaminate-scaled (Ss) and Ply-blocked scaled (Ps) laminates, respectively. Both types of laminates have a nominal thickness of ~ 4 mm.

The specimen geometry was based on the ASTM D7136 standard [26]. Baseline specimens that exactly followed the standard were cut to 100 mm x 150 mm for both Ss and Ps laminates and then submitted to low-velocity impact test, with various impact energies. Large-scale (Ls) specimens, using only the Ps stacking sequence, were cut to 200 mm x 300 mm and tested at various impact energies and impact locations. To accommodate the Ls laminate in the standard impact testing equipment, a new supporting structure was designed and manufactured. The opening dimensions of the larger supporting window were directly scaled up, giving an opening of 250 mm x 150 mm, based on double the standard opening (i.e. 125 mm x 75 mm), however the impactor with diameter of 16 mm was used for both test conditions. The testing configurations are listed in Table 1, and Figure 1 shows the standard and large supporting windows.

In order to be consistent with the previous quasi-static indentation study [14], the impact energies used were controlled to only result in matrix cracks and delaminations, without the

occurrence of fibre breakage and perforation. For each post-impact laminate, the projected delamination area was inspected by ultrasonic C-scanning. In addition, X-ray Computed Tomography (CT) scanning was also performed on selected standard specimens.

Table 1: Configurations of the standard (Ps and Ss cases) and large laminates tested and size of the support openings.

Specimen		Specimen size (mm)	Supporting window opening (mm)	Stacking sequence	Effective ply thickness (mm)	Number of plies
Standard plates	Ply-blocked scaling (Ps)	150 x 100	125 x 75	$[45^\circ_2/0^\circ_2/90^\circ_2/-45^\circ_2]_{2S}$	0.25	16
	Sublamine scaling (Ss)			$[45^\circ/0^\circ/90^\circ/-45^\circ]_{4S}$	0.125	32
Large scale laminate (Ls)		300 x 200	250 x 150	$[45^\circ_2/0^\circ_2/90^\circ_2/-45^\circ_2]_{2S}$	0.25	16

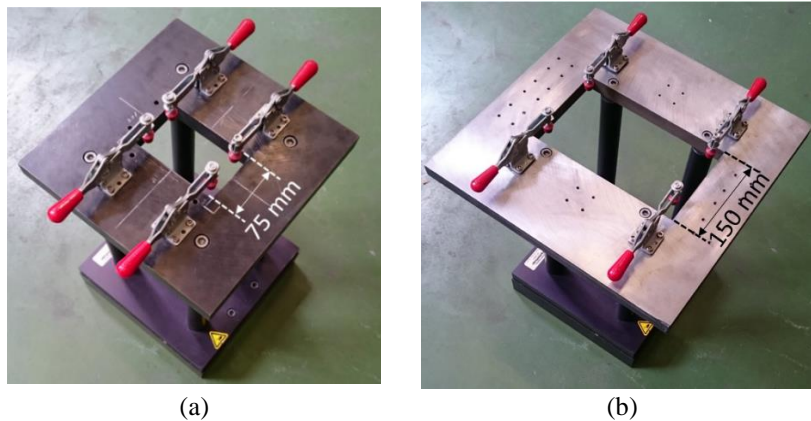


Figure 1: (a) the supporting window for standard size specimen with opening 125 mm x 75 mm. (b) the large supporting accommodating large size laminate impact with an opening 250 mm x 150 mm.

To investigate the effect of the impact location, and hence boundary conditions, on damage and structural response, central and offset impact tests were conducted on the Ls specimens. Figure 2 illustrates the configurations of central impact on the standard plates (i.e. the Ps and Ss cases) and the two offset impacts on the Ls plate. Three impact tests were performed on each Ls plate, one at each location, denoted as the central impact (C-Imp), longitudinal direction offset impact (L-Imp) and the width direction offset impact (W-Imp). The impact energies used were 12 J, 5 J and 12 J, respectively. The effect of boundary conditions on damage extent was expected to be significant for the W-Imp case, so the lowest impact energy

was used for this case (i.e. 5 J) to avoid interaction between delamination and the edges of the plate. Impact locations in Ls plates were designed to be sufficiently far apart so as to avoid interactions between secondary and pre-existing impact damage.

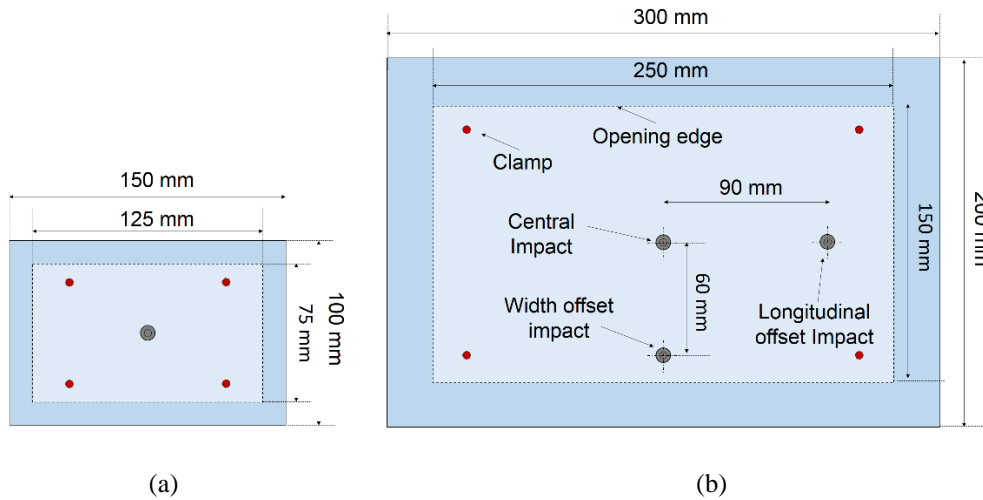


Figure 2: Schematic of the standard (a) laminate size with underlying supporting window opening and the large laminate size (b) with underlying support opening and impact locations (central, longitudinal offset and width direction offset impacts).

3. Modelling Techniques

3.1 High-fidelity Solid (3D) Model

The high-fidelity 3D models used in this study were similar to those developed in the previous quasi-static indentation study [14], in that the same composite laminate model and boundary conditions were used, but here the load was applied dynamically. FE models were pre-processed using the Oasys-Primer software and then solved by nonlinear explicit FE software LS-Dyna.

Ply of the laminate model were modelled with single integration point brick elements (Type 1 in LS-Dyna). 6 strips of intralaminar cohesive elements (Type 19 in LS-Dyna) were inserted vertically in each ply, parallel to the fibre orientation, such that they were evenly spaced under the impactor, at the centre of the plate. These strips of intralaminar cohesive elements simulate major matrix cracks damage during impact. The spacing of strips of intralaminar cohesive

elements was determined from CT-scanning performed in [14]. In addition, layers of interlaminar cohesive elements were positioned between plies with different fibre orientations to predict delamination damage. According to the calculation presented in Harper and Hallett [37] for accurate interface element performance, finer meshes were required in the interlaminar cohesive layers than in the plies. Hence, segment based tied contact was defined between surfaces of adjacent plies and the corresponding layers of interlaminar interface elements between them. The interface element failure algorithm used a quadratic damage initiation criterion and an energy-based propagation criterion, with mixed mode failure being a linear combination of mode I and II. A complete description of the modelling techniques and details of how cohesive elements were placed at inter- and intralaminar locations is given in [14]. The material properties for ply and interface properties used in the model are listed in Table 2. It is noted that an identical set of interface properties were used for both intra- and interlaminar cohesive elements in all of the models in this study. This was deemed appropriate as a number of experimental studies have shown comparable values for intra- and interlaminar properties [38,39]. The enhancement factor (ϕ) essentially serves as an internal friction coefficient that allows the increase of the Mode II interfacial strength and critical energy release rate due to through thickness compression stress and controls the critical load corresponding to the delamination initiation. The value used in this dynamic impact simulation is empirically derived here and higher than that used in the static indentation simulations in [14] because of the strain-rate sensitivity of the friction coefficient [40].

The impactor and supporting window were modelled as rigid bodies. The weight and size of impactor model was configured as to be the same as that used in the experiment (i.e. 6.35 kg weight and 16 mm diameter). The impactor was placed 0.1 mm above the top surface of the laminate model and given an initial velocity calculated from the pre-defined impact energies for the different cases. During the impact simulation, the impactor engages with the plate and

bounces back. The simulation was terminated after the impactor returned to its original position. The model's impact force was derived from the contact force between impactor surface and the top surface of the laminate. The four rubber-tipped clamps were designed to stop the plate moving upwards after impact in the experiment and located inside the boundary of the supporting edges [41]. They should not affect the impact response and damage incurred, so were not included in the simulations.

Table 2: Material properties of IM7/8552 [42,43] (The interface properties listed were used for inter- and intralaminar interface elements)

Ply properties	Interface Properties
$E_{11} = 161 \text{ GPa}$ $E_{22} = E_{33} = 11.4 \text{ GPa}$	$E_I = E_{II} = 100 \text{ GPa}$
$\nu_{12} = 0.3$ $\nu_{23} = 0.436$	$\sigma_I^* = 60 \text{ MPa}$ $\sigma_{II}^* = 90 \text{ MPa}$
$G_{12} = G_{13} = 5.17 \text{ GPa}$ $G_{23} = 3.98 \text{ GPa}$	$G_{IC} = 0.2 \text{ N/mm}$ $G_{IIC} = 0.8 \text{ N/mm}$
$\alpha_{11} \approx 0$ $\alpha_{22} = \alpha_{33} = 3 \cdot 10^{-5}$	$\alpha = 1$ $\phi = 0.58$
$\rho = 1.6 \text{ g/cm}^3$	$\rho = 1.0 \text{ g/cm}^3$

3.2 Solid/shell Modelling Technique

Laminated composites subject to low-velocity impact can be divided into two regions; the first is the highly nonlinear delaminated region and the second is the linear undamaged region [44,45]. The undamaged region plays a key role for load transfer between the boundary and impact site as well as establishing the panel's global response, together with the damaged region. During large-mass low-velocity impact, the geometric (specimen length and width) and boundary (plate edges and boundary conditions) have significant effects on the impact response, and have to be included in the model. This is different from the high-velocity impacts where the response is highly localised, and it may not even be necessary to take the undamaged region into account for virtual testing [46]. The solid/shell coupling approach developed in this work is thus appropriate for any quasi-static and low velocity loading condition, except those where the damage location is not known prior to the simulation.

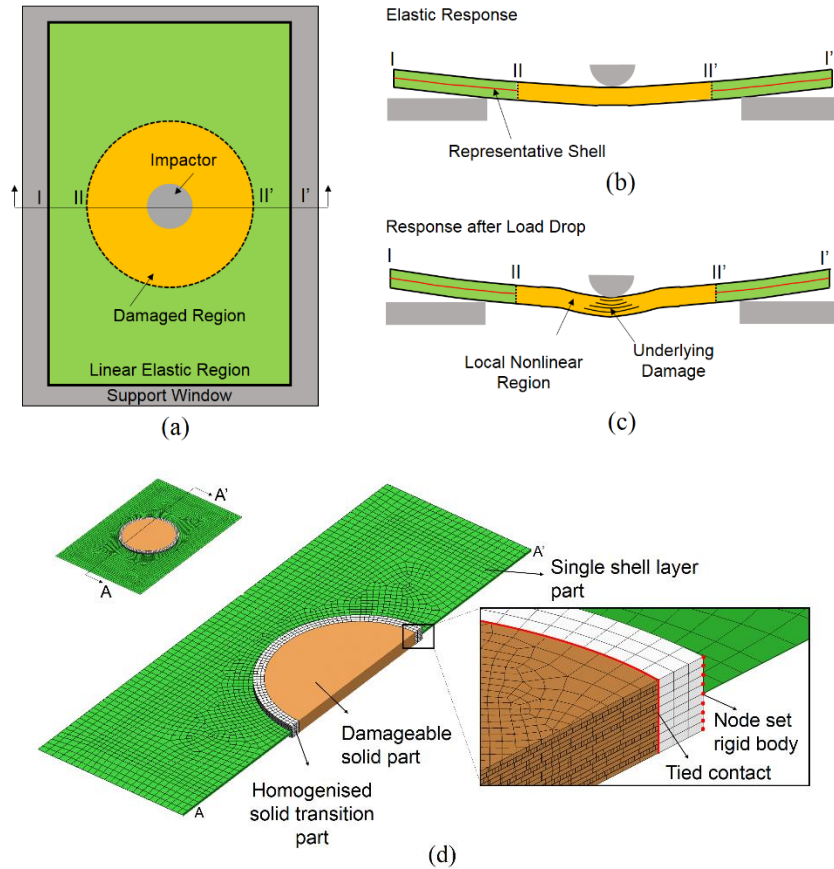


Figure 3: (a), (b) and (c) Solid/shell model in a global/local approach for impact modelling; (d) modelling strategies for integrating high-fidelity solid and shell part into Solid/shell impact model.

Figure 3a, b and c illustrate the global-local approach for low-velocity impact modelling. With the knowledge of the approximate underlying damage size, the laminate can be divided into a potential damage region and an undamaged region, which behaves elastically during the impact event (see Figure 3b). Before delamination initiation, the response of the whole laminate is linear elastic, because the minor matrix cracking and indentation that occurs does not cause significant global stiffness degradation. After the critical load is reached, multiple delaminations grow and lead to the laminate forming multiple sublaminates. These thin sublaminates exhibit strong nonlinearity under transverse loading, and therefore there is a high geometric nonlinearity at the delaminated region (see Figure 3c). This phenomenon has been widely used for obtaining analytical solutions for impact modelling [44,47]. It can be seen that if the size of the damageable region is carefully determined, the only role of the undamaged

region is in transferring the loads and displacements to the damageable region from the boundaries. Shear deformations, through-thickness stresses and membrane deformations have very little effect on the response of the undamaged region that is far away from the transverse loading. This approach conforms to the simplest thin plate theory and in turn the shell theory, as deflections are small. With an efficient coupling mechanism, a single layer of shell elements with equivalent material properties located at the mid-plane of the undamaged region, away from transverse loading and the nonlinear response region, is therefore sufficient to represent the elastic response of the undamaged region of the laminate under transverse loading. In order to model different damage modes at different locations, 3D solid elements are necessary at the potential damage region.

When coupling solid and shell elements in one model, it is of importance to ensure that rotational degrees of freedom (DoF) from nodes of the shell elements are fully transferred to the translational DoF of the connecting nodes of the solid elements. The solid elements used for plies are reduced integration 8-node hexahedron element with a single integration point at the centre of the element with 3 translational DoF at each integration point. For normal shell elements, each integration point has translational and rotational DoF. Therefore, a sufficient number of solid elements in the through thickness direction should be considered in order to transfer rotations to the connecting shell elements. The solid/shell coupling is here implemented using nodal rigid body constraints. Each node on the connecting shell element is rigidly connected to a line of nodes through the thickness on the connecting solid elements at the same in-plane location.

Based on the aforementioned concept, the solid/shell model was developed and is shown in Figure 3d. The full description and characteristics of the damageable 3D solid part in the region of interest were presented in the previous section. The surrounding shell part representing the undamaged region was modelled by computationally efficient shell elements (Type 2 in LS-

Dyna). Each ply was defined as an integration point in the shell normal direction. In order to connect the fine mesh region of the fully damageable 3D solid part in the local domain with the coarse mesh region of the shell layer at the global domain, a ring-shaped mesh transition part consisting of 8 solid elements in the through thickness direction was introduced between the fine mesh solid part and the coarse shell part. A surface-based tied contact was defined between the inner surface of the mesh transition part and the outer surface of the damageable solid part. The transition part had homogenised material properties, equivalent to the multilayer solid part. Nodes at the inner edge of the shell part were merged with the nodes at the mid-plane of the transition part. Each nodal rigid body was defined by a line of nodes (see ‘Node set rigid body’ in Figure 3d) in the through-thickness direction at the inner edge of the shell part (outer edge of the solid transition part), which allows displacement and rotation transfer between local and global domains. However, the line of nodes are rigidly connected, which means any relative displacement between nodes in each nodal rigid body definition is prohibited. Thus, the nodal rigid body complies with the thin plate theory in that the line remains normal to the mid-plane before and after a small deflection. The transverse displacements and rotations of the local solid domain due to impact loading can be effectively transferred to the global shell layer that couples to the mid-plane of the local solid plate. The diameter of the fully damaged solid part (see Figure 3d) was set to 60 mm which is determined by the size of the maximum damage area measured in the ASTM standard impact tests.

To develop efficient and robust numerical models that can represent global behaviour and predicting failure of large-scale composite structures under impact, there is a need for a systematic approach. **Error! Reference source not found.** highlights the work flow used in this study. The 3D high fidelity 3D models were first validated against low-velocity impact experimental results. Standard size ASTM virtual impact tests using the solid/shell modelling technique were then performed, and the numerical results were thoroughly compared with the

previous baseline fully solid model, to ensure a high level of similarity in both global response and damage prediction. Once the modelling technique at the standard coupon scale was validated, the numerical study was moved to the large-scale plate impact modelling to simulate the structural behaviour and associated damage. The numerical results of the large-scale plate models were validated against experimental observations obtained in this study, after which the capability of the modelling approach was further explored, as a case study, by applying it to a large stringer stiffened panel. The modelling results for this structural level component were compared with the experiment results available in the literature [10].

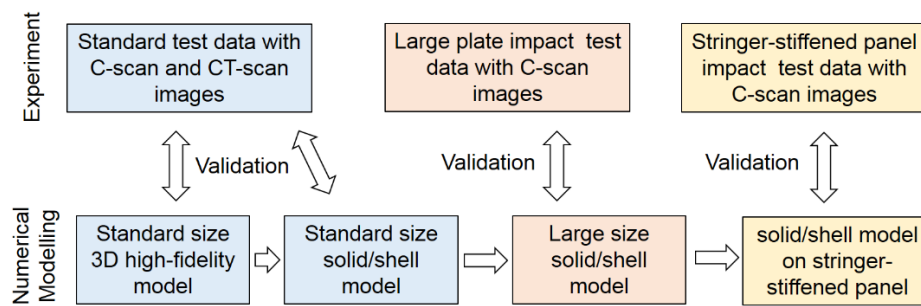


Figure 4: Methodology of numerical modelling from small coupon level to structural component.

4. Experimental Results and Discussions

4.1 Standard Test

Figure 5 shows the impact force history plots of the Ps and Ss cases at the threshold energy (i.e. E_{THLD}). The load drops reflect the delamination initiation, followed by unstable propagation. The threshold impact energy was determined by trial impact tests. Plates impacted with energies lower than the threshold values were confirmed by smooth half sine wave force histories and no detectable damage in the C-scans [48]. The threshold energies for the Ps and Ss laminates are found to be 6 J and 10 J, respectively, which means that the Ss laminates are more impact resistant than the Ps laminates.

Figure 6 shows force history plots of the Ps and Ss laminates under increasing impact energies. Both figures confirm the obvious experimental scatter in the critical load levels between the

different energy tests, and the figures also highlight the trend of the critical load (F_C) in the Ss case being higher than the Ps case, which was also observed in the static indentation tests [14]. In the 16 J Ps case it is noticeable that there is a second load drop on the curve. This corresponds to a second unstable delamination propagation that is observed in the post-impact c-scan results.

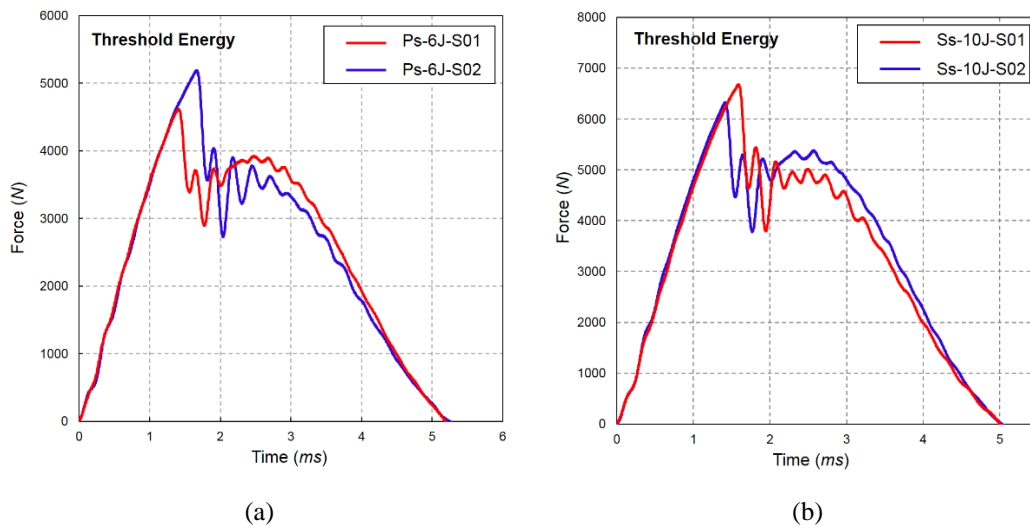


Figure 5: Force history plots for (a) Ps and (b) Ss specimens under low-velocity impact with threshold impact energy. (S01 denotes specimen number).

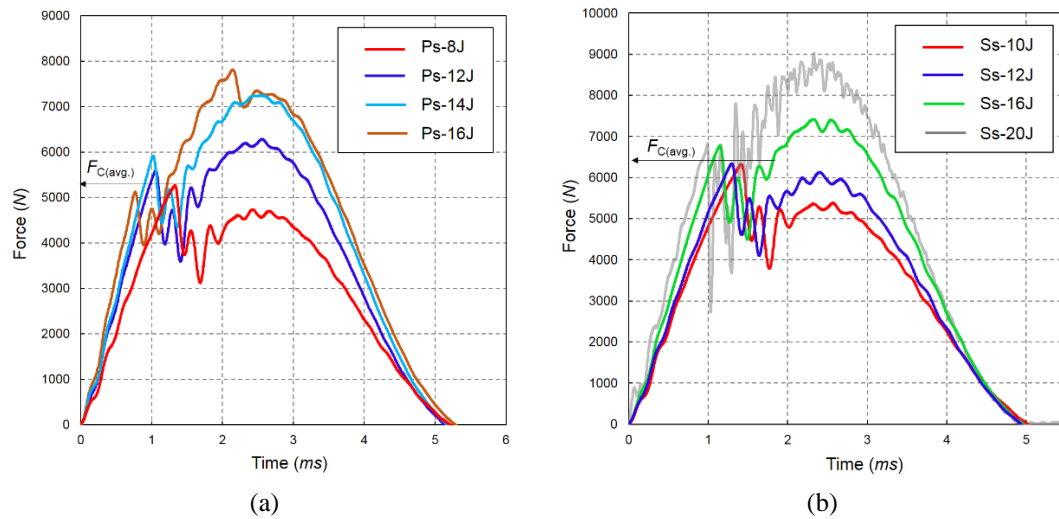


Figure 6: Representative force history plots for; (a) Ps configuration; (b) Ss configuration. The averaged critical load ($F_{C(avg.)}$) is marked.

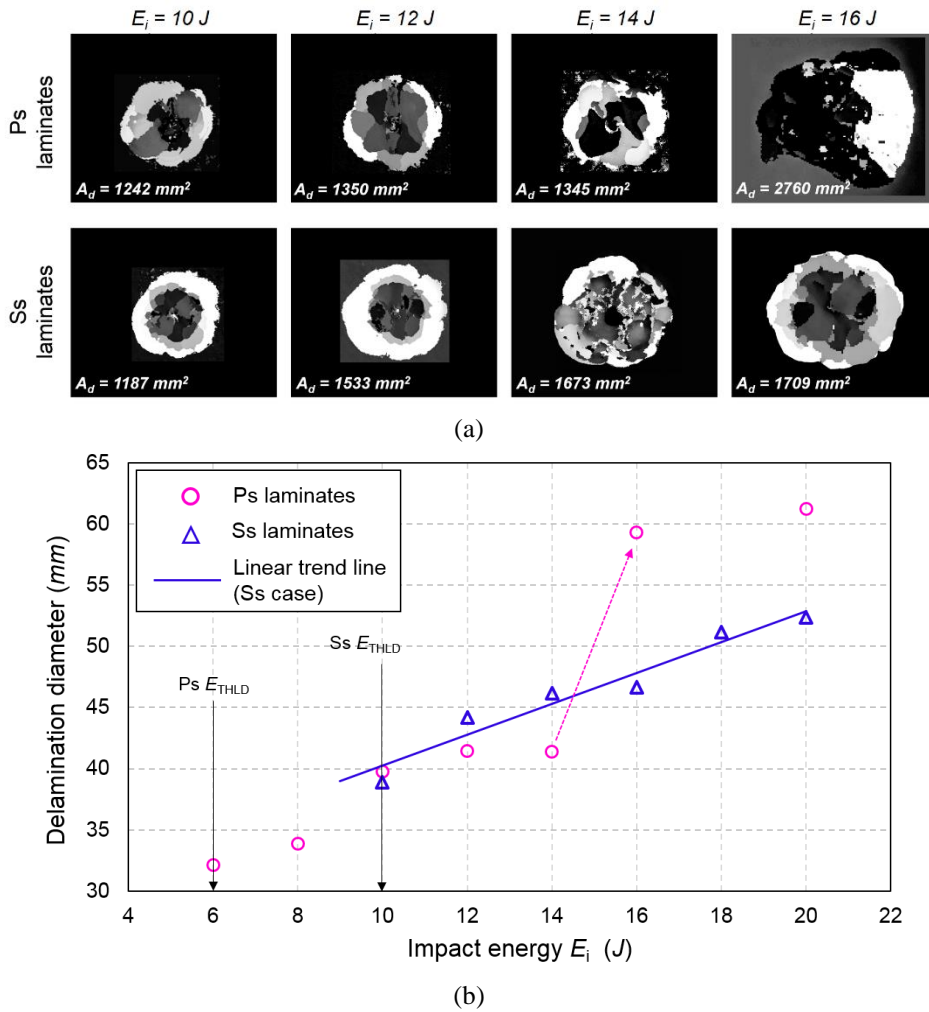


Figure 7: (a) Collection of C-scan images of the Ss and Ps laminate with various impact energies; (b) Delamination diameter comparison between the Ps and Ss case against impact energy. (E_{THLD} denotes the threshold impact energy)

Figure 7a shows a comparison of delamination area measured by ultrasonic C-scan in selected Ps and Ss specimens with different impact energies, and Figure 7b plots the relationship between impact energies and the projected delamination areas in each case. It can be seen that the projected delamination shapes for both laminate types are repeatable and similar to each other for all impact events, except for the case of the Ps specimen under 16 J impact. For the Ps specimen impacts under 16 J or higher, an unstable increase of the delamination area is observed (i.e. the second significant load drop in the force history plot in Figure 6a). In this case, there is significant and unstable delamination growth at some interface(s), which leads to

an asymmetric overall projected delamination shape. For Ps laminates subjected to 20 J impact, the relationship between delamination size and impact energy tends to level off. In contrast, the Ss specimens under the same impact energies (16 J and 20 J) still retain an overall circular delamination area. The stable growth in projected delamination area observed for the Ss specimens once again confirms the fact that Ss laminates are more impact resistant compared to the Ps case.

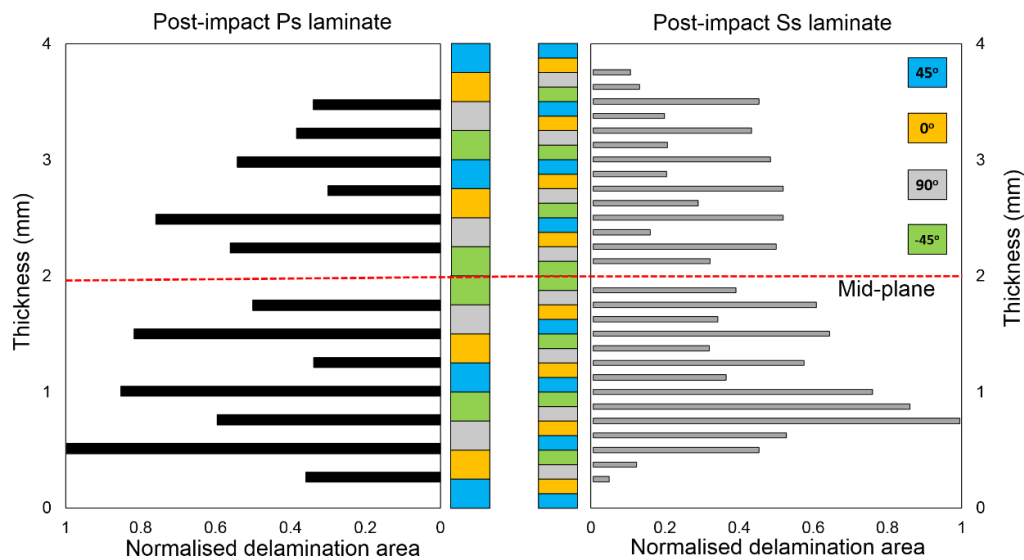


Figure 8: Comparison of detailed individual delamination area in 10 J post-impact Ps and Ss laminates. The delamination area is normalised by the maximum delamination area found in available interfaces.

Selected post-impact Ps and Ss specimens that were impacted at 10 J were submitted to X-ray CT-scanning for detailed damage assessment. The through-thickness information on individual delamination areas of these specimens are compared in Figure 8, normalised by the maximum delamination area found in each case. It can be seen that larger delaminations are found at 90° interfaces (i.e. the angle difference of neighbouring plies), rather than 45° interfaces, for both configurations. The maximum delaminations in both cases occur at 90° interfaces close to bottom surface and are located at a roughly similar through-thickness location, whilst the minimum delaminations are located at the top and bottom interfaces.

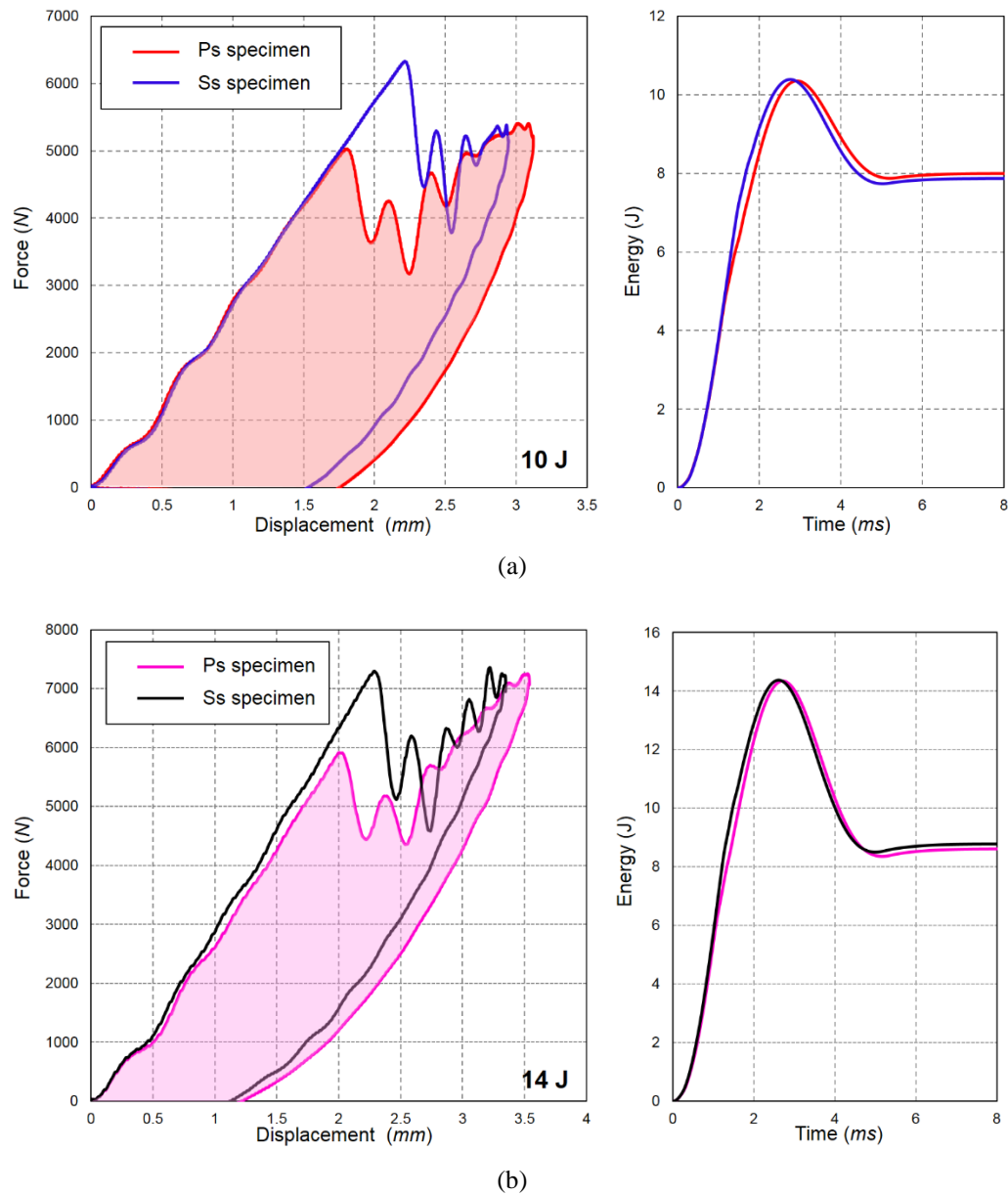


Figure 9: Comparisons of force-displacement plot and energy plot generated from the drop-weight impact tower between Ps and Ss specimen under (a) 10 J and (b) 14 J impact energy.

Ps and Ss laminates under 10 J and 14 J impact energies (see Figure 7a and b) generate similar projected delamination areas. The Ss laminate has nearly twice the number of available interfaces for delamination compared to Ps due to the single ply stacking sequence; hence, the total delamination area of the Ss specimen was expected to be relatively larger than that in the Ps laminate for a given impact energy. Figure 9 shows comparisons of force-displacement plots and energy absorption of the Ps and Ss cases under 10 J and 14 J impacts. As the figure shows, despite the total delamination area of the Ss laminates being larger than the Ps case for given

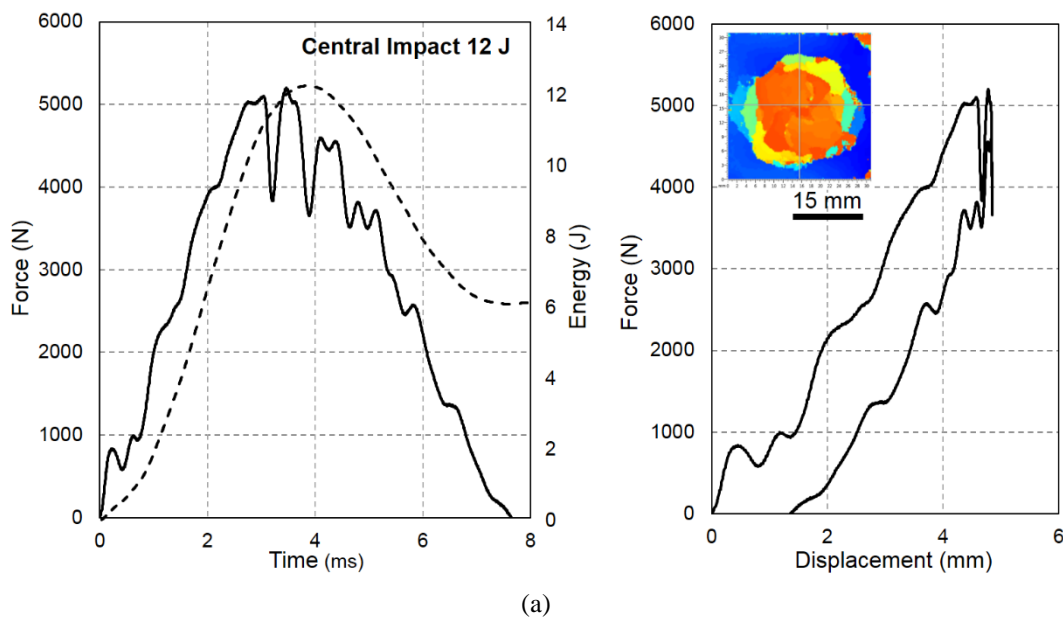
impact energies, the difference in total delamination is not directly reflected by a difference in absorbed energy in these plots. However, Figure 9 and the rest of the force-displacement plots indicate slightly higher amplitude of force oscillations after the load drop in Ss cases compared to the Ps cases. The higher number of delaminations in the Ss case may lead to an increase in the vibration of the laminate during change in stiffness; whereas the Ps case has fewer interfaces, exhibiting a more progressive and smooth change of stiffness than the Ss case. The same behaviours were also reported by González et al [49], where the authors observed a clear difference in the amplitude of the force oscillation after the load drop in three sublaminate scaled laminates under the same impact test conditions. A clear trend of increasing delamination area in three laminate clustering configurations (single- double- and quadruple-blocked ply laminates) under given impact energies was experimentally observed and reported in [50–54]. Here, this trend is not so obvious until the impact energy is higher than 16 J.

4.2 Large Plate Test

One of the key objectives of this study was to characterise the impact response of composite plates as the size increases and impact location changes. The offset impact tests allow one to investigate the correlation of impact damage with differences in boundary conditions under a given impact energy. The results from this section were also used to evaluate the solid/shell numerical modelling techniques for larger structures.

Figure 10a, b and c shows the force/energy histories, force-displacement plots and C-scan image of delamination for central (C-Imp), longitudinal offset impact (L-Imp) and width offset impact (W-Imp) events, respectively. The impact force history and duration vary as the impact location and boundary condition change, although it is notable that the force at first load drop remains fairly consistent at about 5 kN, with similar delamination areas. There is also a slight

change in shape of the delamination in the W-Imp case to oval instead of circular, as shown in Figure 10, due to changes in the boundary conditions. The stiffness variation can be explained by the boundary conditions and the distance between impact location and the nearest support window edge. The W-Imp case (see Figure 2b) has the stiffest response and shortest impact duration. For the same reason, there is also less force oscillations (see energy plot in Figure 10c). In contrast, the C-Imp case exhibits force oscillations at the very beginning of the impact. Despite the changes in boundary conditions hence the stiffness of the response, experimental results show that first delamination occurs at an approximately constant force and gives largely the same area in all cases. These observations are in line with the statements from Davies and Zhang [55] who identified the critical force is the most important parameter, driven by material property and being independent of size and shape of the laminates.



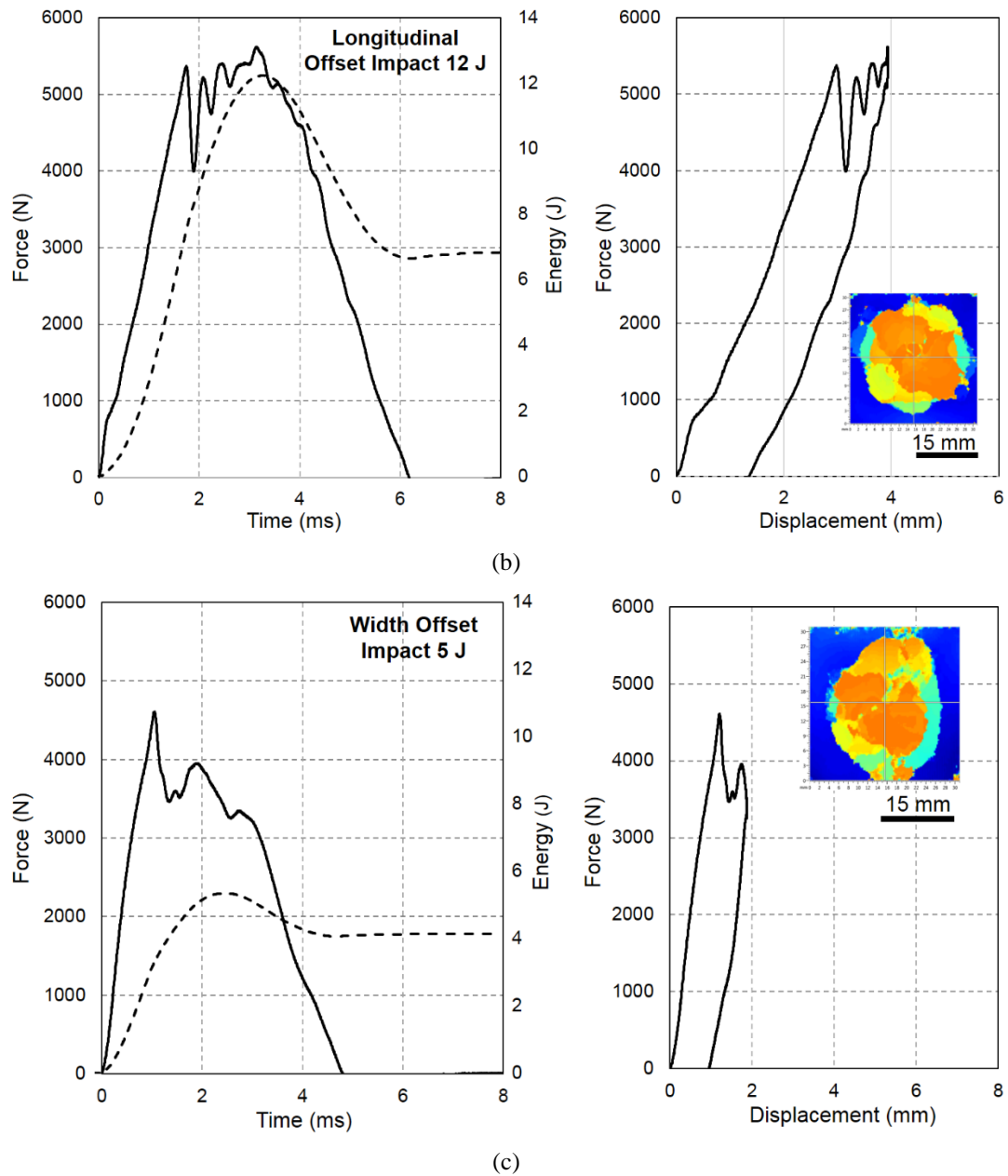


Figure 10: Force and energy histories and force-displacement plots for; (a) central impact under 12 J energy, (b) longitudinal offset impact under 12 J energy and (c) width offset impact under 5 J energy. The dashed line at the LHS of each plot indicates the energy history.

5. Numerical Model and Validation

5.1 3D Solid Model of ASTM Standard Impact

In this section, the numerical results of the fully solid model are compared and validated against the experimental observations, including force history, energy absorption and damage assessment from ultrasonic C-scanning and CT-scanning.

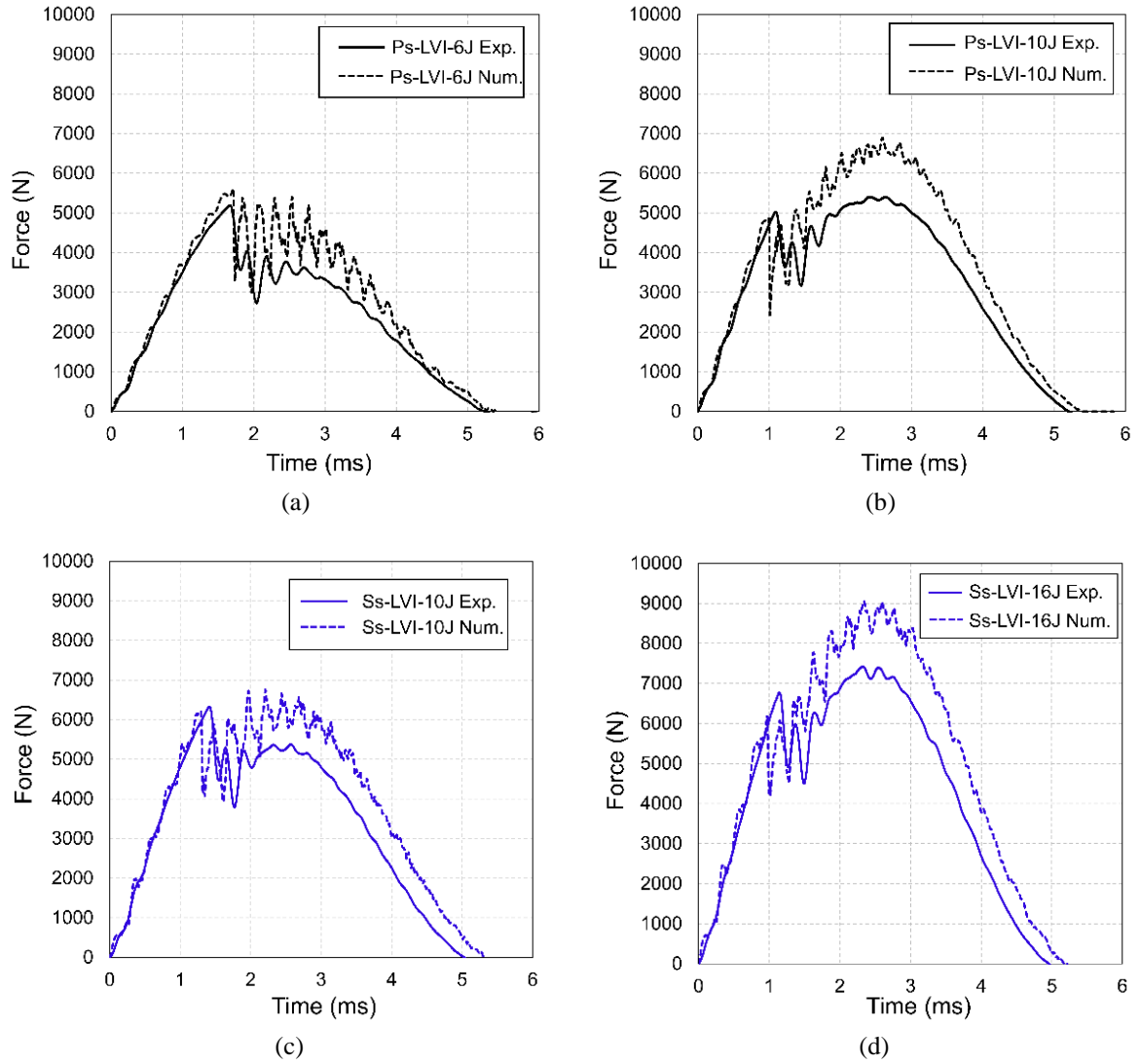


Figure 11: Comparison of force histories in low-velocity impacts (LVI) between experimental and finite element results (a) Ps laminate under 6 J impact; (b) Ps laminate under 10 J impact; (c) Ss laminate under 10 J impact; (d) Ss laminate under 16 J impact.

Figure 11 compares the force histories of numerical and experimental results for Ps and Ss laminates. Two impact simulations were performed for each Ps and Ss case; one at the delamination threshold energy (i.e. 6 J for the Ps case and 10 J for the Ss case) and the other at a higher energy (i.e. 10 J for the Ps case and 16 J for the Ss case). The figures show that the critical load levels predicted by the 3D solid model are consistent with the experimental results for each laminate configuration and are insensitive to the impact energy levels; the difference between the predicted and experimental results on critical load are less than 7% for both laminate configurations. The numerical models also capture the magnitude of the load drop reasonably well. Each force oscillation associated with the interaction between plate vibrations

and delamination propagation is well captured by the impact models at the correct frequency, but the magnitude and duration is slight larger in the simulations compared to the test results, since no damping was used in the model. The higher critical load in the Ss laminate (as compared to Ps), is correctly captured and can be attributed to the same sublaminar-scaling effect that was described in [14].

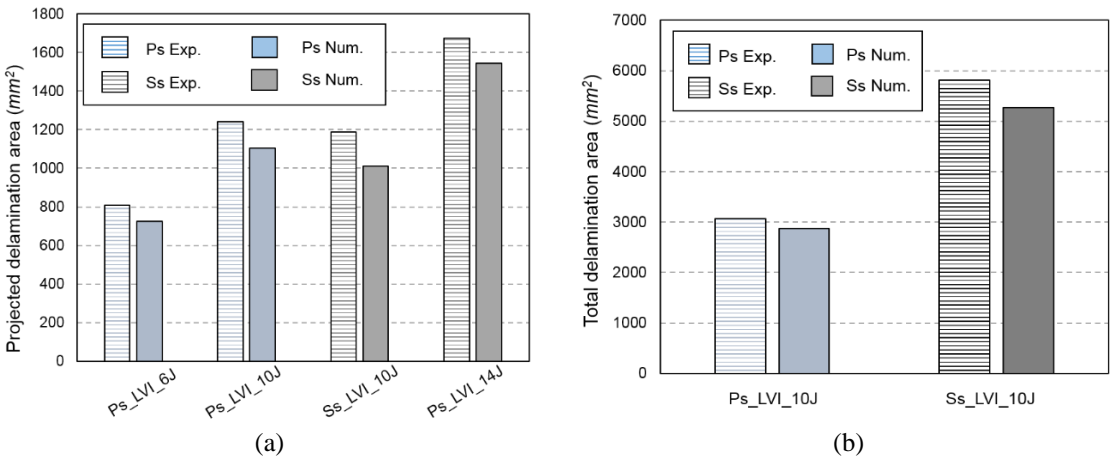
The impact durations for all cases are well captured with a difference of less than 5%. The overall peak impact force (after first load-drop) is related to the residual flexural stiffness of the delaminated laminate, as well as the residual kinetic energy of the impactor. The peak force predictions are consistently higher than the experimental results for both cases in both impact conditions. This is likely to be because not every single damage event and energy dissipation mechanism is captured in model. If one compares the energy absorbed in these low velocity impacts with the quasi-static indentations from [21] using the area under the force displacement curve (see Table 3), it can be seen that, for a similar delamination size, the quasi-static case absorbed energy is much lower. The predicted absorbed energy from the low velocity impact models is much closer to the quasi-static case in this comparison, thus indicating that a significant amount of impactor kinetic energy loss can attributed to energy dissipation mechanisms other than dissipated in creating matrix cracks and delaminations, since in all three cases the damage levels are very similar. The prediction of the energy loss during the impact testing was not the primary concern of this work and this lack of correlation is not seen as significant.

420

Table 3: Energy absorption comparison between FE and experimental results.

Laminate configuration	Impact energy (J)	E _{ab} Exp. (J)	E _{ab} of static indentation tests with the similar delamination size (J) [14]	E _{ab} Num. Impact (J)
Blocked-ply laminate (Ps)	6	4.96	2.98	2.34
	10	7.95	3.0	2.95
Sublaminate scaling laminate (Ss)	10	8.20	3.11	3.36
	14	8.77	4.1	3.92

421



422

Figure 12: Comparison between numerical and experimental results for the Ps and Ss cases; (a) projected delamination area for 6 J, 10 J and 14 J low-velocity impacts (LVI); (b) total delamination area for 10 J impact.

424

425

The projected and total delamination areas of the Ps and Ss laminates after impact were

426

measured by C-scan and X-ray CT scan respectively and compared with FE model predictions

427

in Figure 12. In general, the predicted delamination areas are slightly smaller than the

428

experimental results. However, the underestimations are within 10%. This also reflects in the

429

overestimation of the predicted peak force, indicating less loss of compliance, which would be

430

expected to improve if the predicted delamination area was closer to the experimental result.

431

The projected delamination area is influenced by the large individual delaminations at the lower

432

90° interfaces (see Figure 8) which overshadow smaller delaminations at 45° interfaces. When

433

comparing the trend of delamination area growth from 6J to 10J for the Ps case, and 10 J to 14

434

J for the Ss case, the high-fidelity FE models capture the development of delamination very

435

well. Figure 12b compares the total delamination area derived experimentally from CT-scans

(also see Figure 13) and numerically from the Ps and Ss cases under 10 J impacts. The predicted total delamination area correlates with experimental results even better than the projected delamination area.

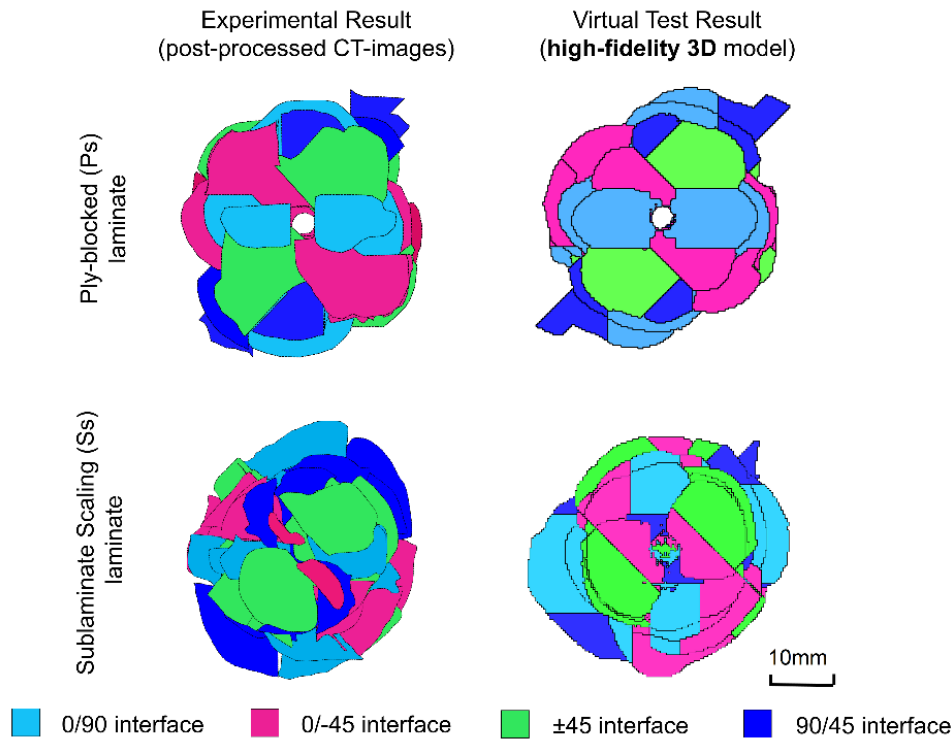


Figure 13: Comparison of projected delamination area between FE models and CT-scan images for Ps and Ss specimen under 10 J impact. Note that the interface is position from top (impact surface) to down (back surface).

Two impacted specimens, the Ps and Ss laminates under 10 J impacts were submitted to X-ray CT-scanning to provide the full detail of delamination damage and to further validate the predictive capability of the numerical models. From the comparison in Figure 13, it can be seen that the models capture the overall delamination size very well, and also the large delaminations at 90° interfaces (in cyan) and some of the delaminations at 45° interfaces (in blue and magenta) at the lower half of the laminate.

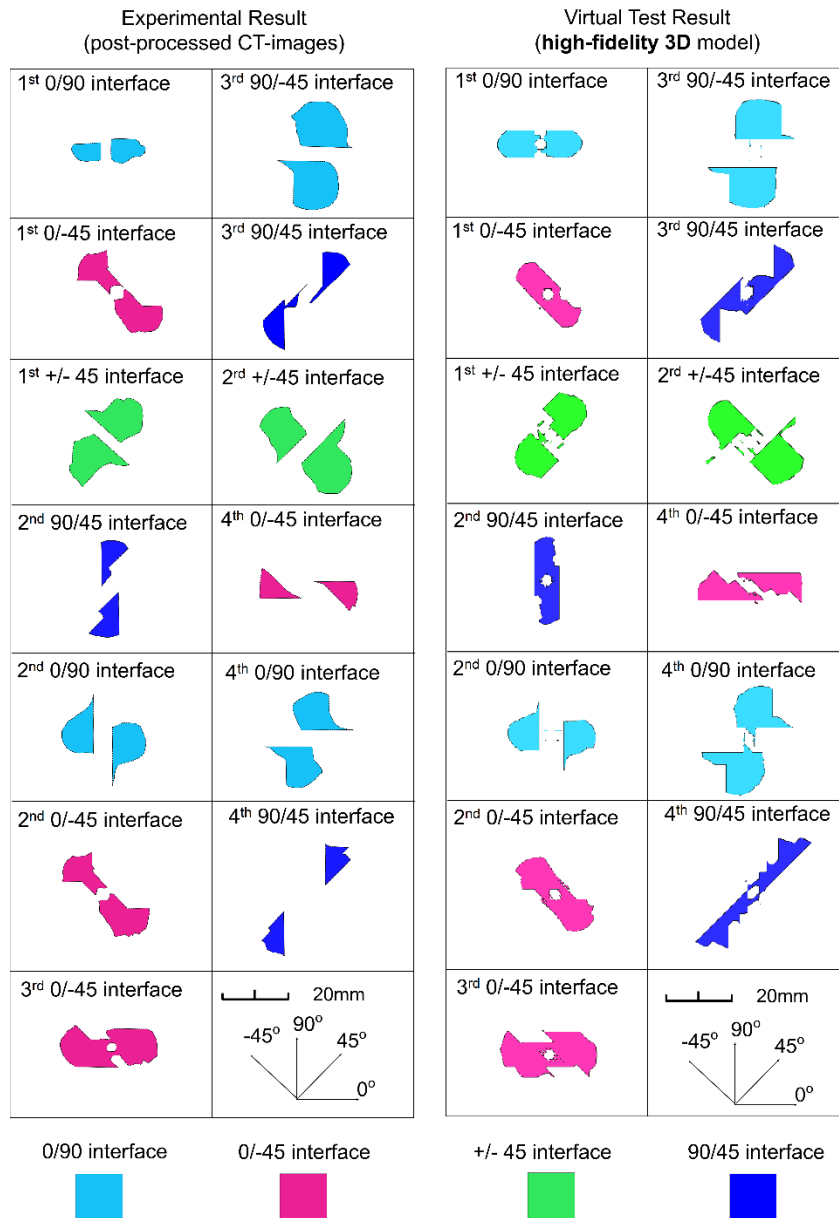


Figure 14: Individual delamination comparison between CT-scan images and FE predictions of high-fidelity 3D solid model at each interface in the case of Ply-block scaling (Ps) laminate under 10 J impact.

Figure 14 compares the individual delaminations at the different interfaces between the 3D solid model and post-processed CT-images for the Ps laminates under a 10 J impact. The individual delamination shapes, sizes, and delamination free zone captured by the FE model are in good agreement with the CT-scan images, especially for the ‘peanut’ shaped delaminations on the 90° interfaces. Some of the delamination shapes, such as the 45° interfaces, are somewhat larger compared to experimental results, and some of the delamination predictions near the delamination free zone (centre of the plate) are slightly underestimated.

Once again, this could be caused by the experimental scatter of the low-velocity impact testing and limitations of the current modelling approach. However, these small deviations do not significantly influence the overall laminate response and energy dissipation. The individual delamination predictions in the dynamic case are very similar to the predictions from the static loading condition that was presented in [14], which further proves the robustness of the high-fidelity 3D solid modelling approach in both static and dynamic conditions.

5.2 Solid/shell Model Validation

5.2.1 ASTM Standard Impact

To validate the solid/shell model and to confirm if solid/shell modelling can be a direct replacement for 3D solid models, the ASTM standard size test was modelled as described in section 3.2 and compared to results from the high-fidelity fully solid model.

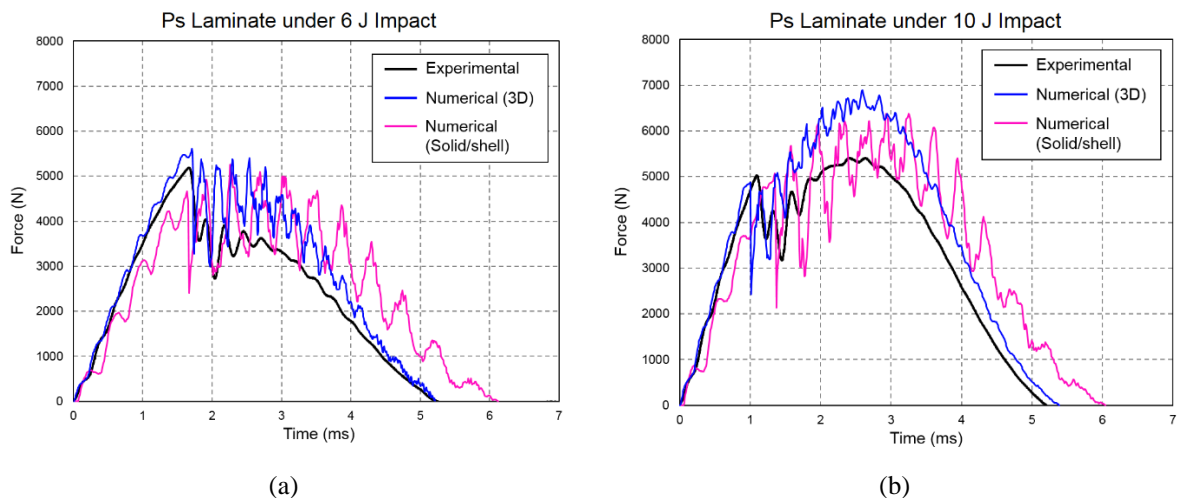


Figure 15: Comparison of ASTM standard experimental and numerical results of the Ps case; (a) under 6 J impact and (b) under 10 J impact.

Figure 15 shows comparisons of force histories between experimental and two numerical results of the Ps case under two impact energies. Generally, the solid/shell simulations agree with both the fully solid and experimental results. The force drop attributed to the development of damage and the interaction with the flexural wave during impact are captured. In addition, the predicted critical load and maximum impact load are similar to experimental results. However, it is apparent that the solid/shell models slightly overestimate the post load-drop

force history, as was the case for the fully solid model. This is because only localised matrix cracks and delaminations are modelled for both cases, overestimating the residual stiffness of the plate after initial damage. When looking at the time required to reach maximum force and the impact completion, the solid/shell models is less responsive than the fully 3D model. This could be attributed to minor coupling effects between solid and shell parts. In addition, due to the additional degrees of freedom in the shell part and the coupling effects, the force oscillations after the damage initiation in Solid/shell models are more severe compared to the 3D solid models.

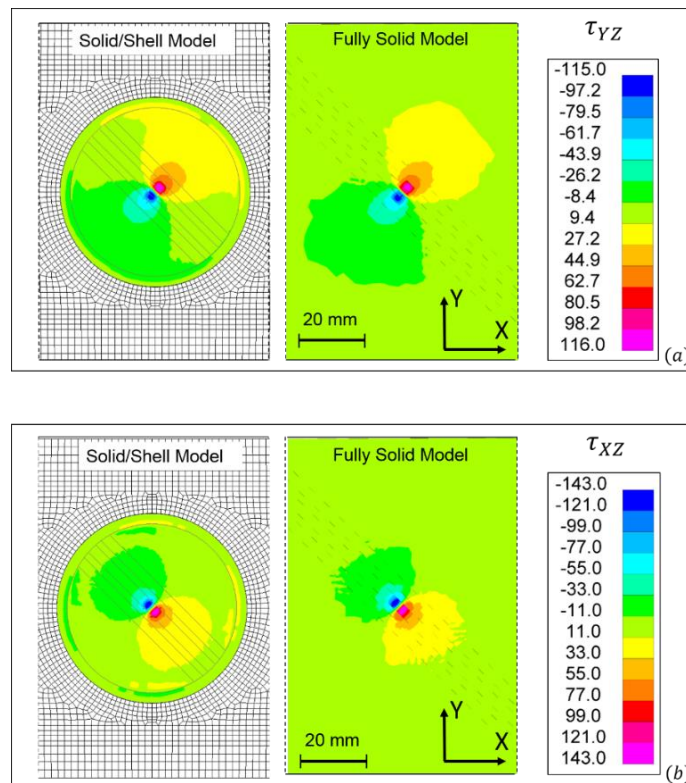


Figure 16: Comparison of interlaminar stressess level of the mid-plane ply in Solid/shell model and fully solid high-fidelity models; (a) τ_{YZ} and (b) τ_{XZ} .

It has been suggested from numerical [14] and analytical [56] modelling that the delamination causing the critical load drop starts at the interface closest to the mid-plane, where the interlaminar shear stresses are highest [55]. The through thickness shear stresses (τ_{XZ} & τ_{YZ}) in the mid-plane ply are thus the governing parameters for the correct prediction of

delamination damage. Figure 16 illustrates the contour plots of the through thickness shear stress components of the mid-plane ply in the solid/shell and fully solid high-fidelity models before damage initiation (the peak values exceed the interface shear strengths in table 2 due to the compression enhancement effect). There is some interaction between the stress field and the solid-shell transition, which is expected due to the inclusion of the homogenised solid transition part. In general, it is clear that the stress levels of solid/shell model at mid-plane correlate very well with the full solid high-fidelity model in the critical region under the impactor. The stress levels in regions away from centre will have little effect on damage predictions due to their low magnitude.

There is also good agreement in the global damage prediction, as shown in Figure 17. This figure compares the projected delamination area measured in experiment (i.e. CT-scan images); the fully solid model and solid/shell model, all at 10 J impact for the Ps laminate. The projected delamination shape, size and distribution in the fully solid and solid/shell model are in close agreement to each other and similar to the experimental observations. The delamination area is slightly underestimated in the solid/shell model, which could be due to the number of DoFs in shell elements leading to a more flexible response compared to the equivalent 3D solid. This can also explain the smaller delamination-free zone in the solid/shell model compared to 3D model.

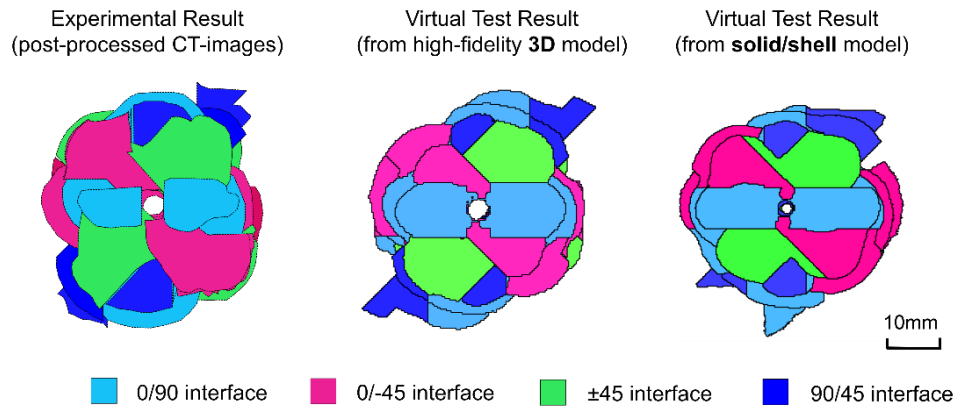


Figure 17: Comparison of detailed delamination between CT-scan, fully 3D high-fidelity and Solid/shell models under 10J impact.

The main advantage of the solid/shell model is the higher computational efficiency compared to the 3D solid model. Factors like number of elements (integration points), contact formulations, dynamic effects and the implementation of user sub-routines can dramatically increase the computational cost of nonlinear explicit FE analyses. Cohesive elements typically require a fine mesh, with at least three elements in the process zone. According to the equations from [37], a cohesive length of ~ 0.2 mm is required for the current material system. Replacing part of the solid element high-fidelity mesh with a single layer of shell elements in the undamaged region, effectively reduces the number of elements. To evaluate the computational cost, high-fidelity 3D and solid/shell models were computed through the University of Bristol's Linux HPC cluster (2 high-memory nodes, with 32 CPUs in total). The completion time and memory required for the solid/shell model in the ASTM standard impact virtual testing were reduced by 50% and 37% respectively, compared to the 3D solid model. Table 4 provides a summary of the total number of elements used in each model developed in this study. It can be seen that the number of solid and cohesive elements of 3D models are significantly reduced and replaced by reasonable number of shell elements in solid/shell model. If the size of the damageable region stays constant, then the larger the part, the more efficient this method becomes.

Table 4 Summary of total number of elements used in each model developed in this study.
Elements with rigid body property are excluded in here.

No. of element	High-fidelity 3D models		Solid/shell models Ps	Large plate impacts		
	Ps	Ss		Central	L-Imp	W-Imp
Solid	182,216	290,480	195,178	195,178	195,178	195,178
Cohesive	1,356,796	2,907,624	764,696	764,696	764,696	764,696
Shell	N/A	N/A	2,444	7809	8784	8970

5.2.2 Large Scale Impact

One of the key objectives of this study was to characterise the impact response of composite plates as the boundary conditions change with increasing structural scale and to capture this through an efficient modelling technique. The impact tests on the scaled-up ASTM standard impact test, reported in section 4.2, allow validation of the solid/shell modelling technique for large flat plates with various impact locations and energies (see **Error! Reference source not found.**).

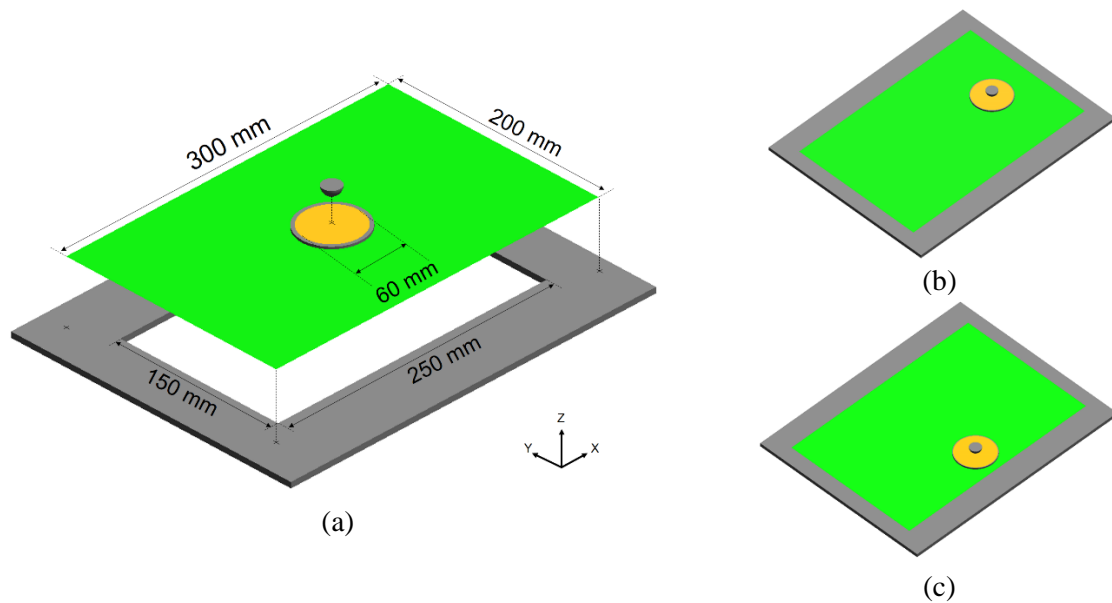


Figure 18: Solid/shell FE model overview. (a) central impact; (b) longitudinal offset impact (L-Imp); (c) width offset impact (W-Imp).

For modelling of the large-scale (Ls) composite plates using the solid/shell approach, the global shell part in the ASTM sized models can simply be scaled up to the relevant dimensions. An

overview of the Ls solid/shell models for the three different impact locations is illustrated in Figure 18. Because the maximum impact energy used in the Ls impact tests is lower than that used in the benchmark tests, the maximum delamination area induced in the Ls tests was expected to be less than the area of the 3D solid part in the solid/shell models. Impact conditions and parameters used in the virtual environment are the same as that in actual Ls impact tests. The modelling techniques and material models used for the Ls impact simulations were the same as those used in the standard ASTM solid/shell model (see Table 2).

Figure 19a, b and c show the comparisons of modelling and experimental force history plots for the C-Imp, L-Imp and W-Imp cases, respectively. It can be seen that the critical load, impact duration and impact force variations are all well captured by the solid/shell model for each configuration. Similar to the trend shown in Figure 15 for the ASTM standard case, the solid/shell models seem less responsive compared to the experiments and have longer impact durations. Again, this could be due to the coupling effects at the boundary between solid and shell parts. However, each force oscillation and the general responses seem to be better captured than for the ASTM standard case. This implies that there is less interaction between the solid-shell element interface and global response as the relative sizes of the two regions decreases. Figure 20 shows a comparison of delamination areas between prediction and C-scan images for all cases. The overall damage predictions of the solid/shell Ls models correlate with experimental results well. The predicted damage in the central and longitudinal offset impact cases are slightly underestimated. In the width offset impact case there is a better damage prediction.

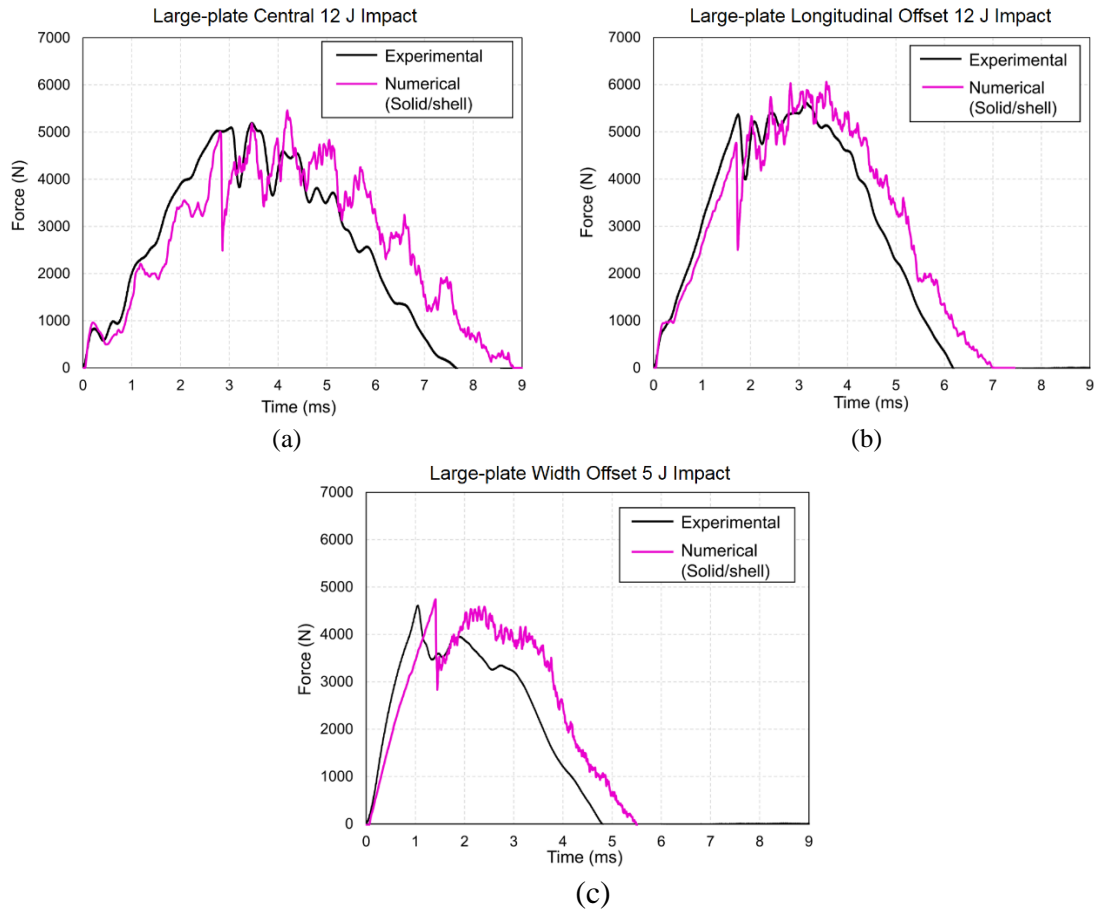


Figure 19: Comparison of force histories of experimental and numerical results in (a) central (C-Imp) 12 J impact test; (b) longitudinal offset (W-Imp) 12 J impact test; (c) width offset (W-Imp) 5 J impact test.

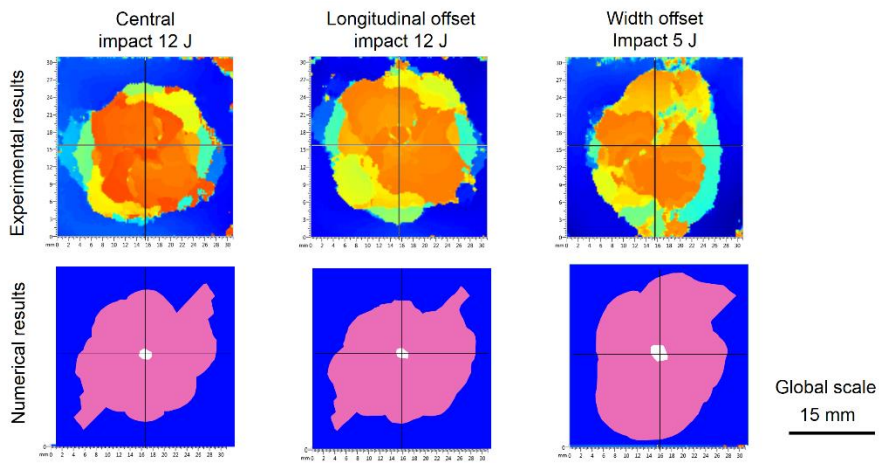


Figure 20: Comparison of projected delamination area observed by C-scan and obtained by numerical modelling.

5.2.3 Complex Structure Impact

To finally show the extent of modelling capability that can be achieved with the solid/shell technique, it was applied to a large and complex composite stringer stiffened panel. The geometry of the structure and material properties were taken from a previous study presented in the literature, which provided experimental results and numerical model validation [10,57]. Here, similar to the standard and large-scale laminate models, the potential damage region was modelled by fully damageable solid part, with a single layer of shell elements elsewhere in the panel, to represent the global behaviour. The geometry and lay-up of the stiffened panel are illustrated in Figure 21. Each stringer was made from three laminates, having two ‘C’ sections placed back-to-back, and the third laminate placed at the top of the two ‘C’ sections as a stringer cap. The stringer is modelled by three separate layers of shell elements, each representing one of the stringer laminates, connected via coincident nodes. The material used was HTA/6176C, and the basic mechanical properties of the laminae and interfaces were taken from [57,58]. Figure 21 also provides an overview of the FE model. The impact event occurs in the middle of the skin bay with 15 J impact energy. The nodes at the ends of the panel were fully fixed in the X direction, to simulate the clamped boundary condition. Here the modelling of debonding between skin and stringers was excluded from this study, but could easily be added via additional cohesive elements at selected locations. The mesh size increased from 0.2 mm at the damageable region to 4.75 mm at the undamaged skin and all stringers. All nodes in the undamaged region, including the undamaged skin and all stringers, could thus be merged together without any form of tied contact.

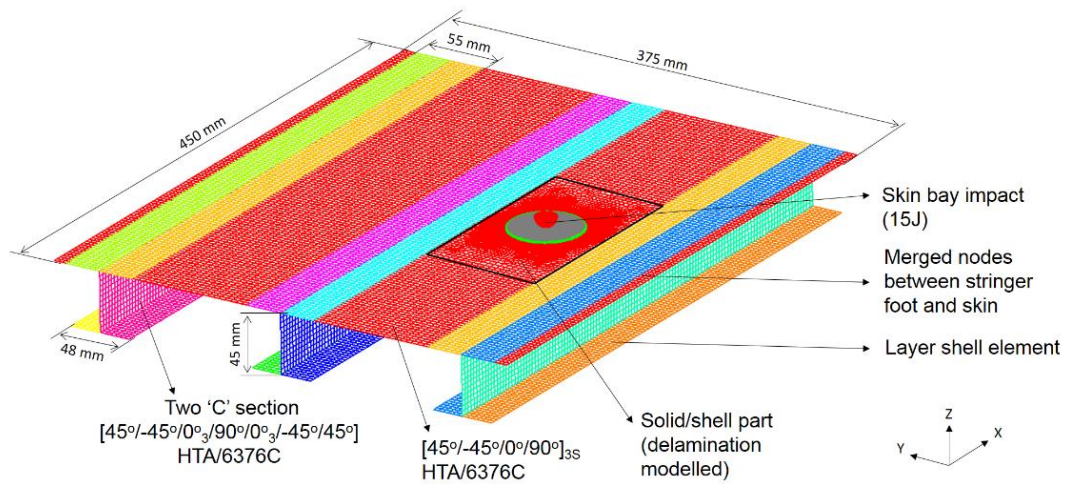


Figure 21: Overview of FE model of the stiffened panel with solid/shell part embedded at the impact location.

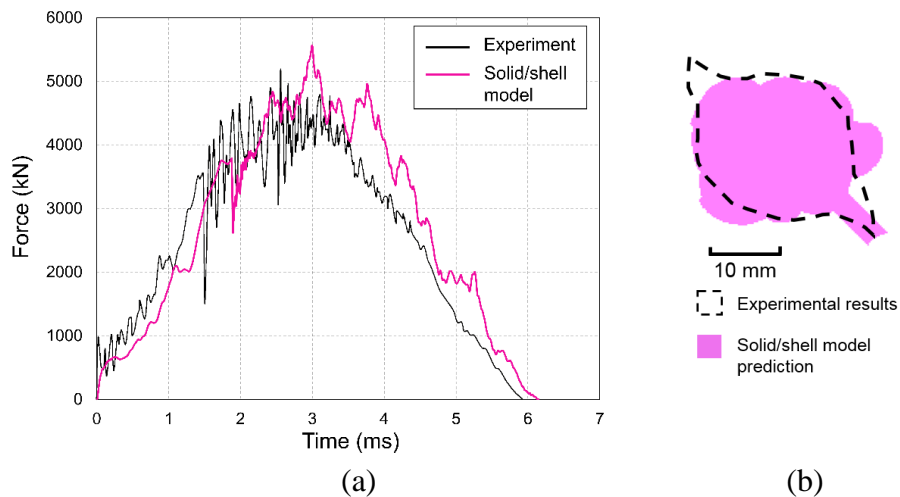


Figure 22: (a) comparison of force history plot of experimental results [57] and Solid/shell model results; (b) comparison between c-scan image of delamination damage from [57] and prediction from Solid/shell model.

Numerical results from the solid/shell model of the stringer stiffened panel were compared to experimental results from [57]. These comparisons include force history and projected delamination size. Figure 22 shows the force history plots of the experimental and modelling results. Similar to the solid/shell models in the previous section, the model appears to be less responsive than the experimental results. The predicted first significant load drop, indicating the delamination onset, was 9% higher than the experimental results (i.e. 3809 N in simulation

and ~ 3500 N in experiment). Because of the steel impactor vibration and its interaction with geometric features and the flexural wave, the oscillatory behaviour of the impact force in the experiment was not accurately captured in the solid/shell model. This is because the predicted force is the contact force and the impactor was modelled with a rigid material, without stress update. However, most of the local peak impact forces, indicating the structural responses, are well captured by the model. The prediction of the peak impact force is slightly overestimated at 5590 N in the model compared to ~ 5200 N in the experiment. This may be because other damage modes apart from matrix cracking and delamination were not taken into account in the damage prediction. The bottom ply fibre direction tensile stress predicted in the model at the moment of maximum deflection slightly exceeded the material strength level (see Table 1 in [10]), which may explain the slight overestimations in delamination area and peak impact force, as shown in Figure 22b. However, the observation of fibre failure in the original experimental results published in [57] was not confirmed.

In general, the correlation between experimental results and modelling results in regards to global impact behaviour and damage extent was very good. This preliminary case study shows the potential of the solid/shell approach. It is possible for this approach to be adapted to large and complex structures whilst giving good damage prediction. The circular high-fidelity solid part for damage simulation can be easily moved to other locations for a complete impact damage vulnerability study. In addition, the shell and solid element peripheries (i.e. the transition part) can conveniently be incorporated within parts of any shape and curvature. The secondary failure mechanism, that is, the interfacial behaviour between the panel skin and stringer foot also can be analysed by inserting cohesive elements between susceptible regions.

6. Conclusions

The work presented here has investigated the low-velocity impact damage resistance of scaled composite laminates, as well as demonstrating the robustness of high-fidelity 3D solid finite

element modelling in a dynamic impact environment. A clear difference in critical load between single-ply (Ss) and blocked-ply (Ps) laminates was observed. The higher critical load in the Ss laminate leads to a higher delamination threshold and delays the delamination propagation in most of the impact events. The difference in delamination area between the Ss and Ps cases appeared to be insignificant for the lower impact energies used, until unstable delamination growth occurs in the Ps case at higher impact energies. These observations are consistent with a previous study that used equivalent quasi-static indentations. High-fidelity 3D FE models were presented and validated by highly detailed experimental observations. The structural responses and detailed damage predictions were in a good agreement with experimental results.

This high quality numerical prediction capability is not however suitable for analysis of low velocity impact on composites with in-plane scaling, to larger structural dimensions. Such analyses are necessary to capture the effects of boundary conditions in relation to the impact locations, to predict the damage threshold and global structural response. This drove the development of a coupled solid/shell modelling technique. This was adopted to model several impact events and was systematically validated by low-velocity impact experiments on ASTM standard plates and larger scale structures. This demonstrated an efficient modelling approach that not only provides high-fidelity predictive capabilities but also retains modest computational costs. In addition, from the experimental observations of this paper and the previous study [14], it can be concluded that static indentation tests can provide a suitable substitute for low-velocity impact tests for composite laminates, at least within the impact energy range tested.

In future work the modelling will be extended to include other failure modes, such as fibre failure, and applied to further cases, such as curved composite structures.

7. Acknowledgement

The testing of the scaled up composite laminates was conducted as a part of the ‘Unlocking the science for an Autonomous Structural Health Monitoring System’ project supported by the GW4 Alliance, UK.

8. References

- [1] Sepe R, De Luca A, Lamanna G, Caputo F. Numerical and experimental investigation of residual strength of a LVI damaged CFRP omega stiffened panel with a cut-out. *Composites Part B: Engineering* 2016;102:38–56.
- [2] Maio L, Monaco E, Ricci F, Lecce L. Simulation of low velocity impact on composite laminates with progressive failure analysis. *Composite Structures* 2013;103:75–85.
- [3] Kim E-H, Rim M-S, Lee I, Hwang T-K. Composite damage model based on continuum damage mechanics and low velocity impact analysis of composite plates. *Composite Structures* 2013;95:123–34.
- [4] Feng D, Aymerich F. Finite element modelling of damage induced by low-velocity impact on composite laminates. *Composite Structures* 2014;108:161–71.
- [5] Shi Y, Pinna C, Soutis C. Modelling impact damage in composite laminates: A simulation of intra- and inter-laminar cracking. *Composite Structures* 2014;114:10–9.
- [6] González EV, Maimí P, Camanho PP, Turon A, Mayugo J a. Simulation of drop-weight impact and compression after impact tests on composite laminates. *Composite Structures* 2012;94:3364–78.
- [7] English SA, Briggs TM, Nelson SM. Quantitative validation of carbon-fiber laminate low velocity impact simulations. *Composite Structures* 2016;135:250–61.
- [8] Lopes CS, Sádaba S, González C, Llorca J, Camanho PP. Physically-sound simulation of low-velocity impact on fiber reinforced laminates. *International Journal of Impact Engineering* 2015:1–15.
- [9] Tan W, Falzon BG, Chiu LNS, Price M. Predicting low velocity impact damage and Compression-After-Impact (CAI) behaviour of composite laminates. *Composites Part A: Applied Science and Manufacturing* 2015;71:212–26.
- [10] Faggiani A, Falzon BG. Predicting low-velocity impact damage on a stiffened composite panel. *Composites Part A: Applied Science and Manufacturing* 2010;41:737–49.
- [11] Lopes CS, Camanho PP, Gürdal Z, Maimí P, González EV. Low-velocity impact damage on dispersed stacking sequence laminates. Part II: Numerical simulations. *Composites Science and Technology* 2009;69:937–47.
- [12] Hallett SR, Green BG, Jiang W-G, Cheung KH, Wisnom MR. The open hole tensile test: a challenge for virtual testing of composites. *International Journal of Fracture* 2009;158:169–81.
- [13] Hallett SR, Jiang W-G, Khan B, Wisnom MR. Modelling the interaction between matrix cracks and delamination damage in scaled quasi-isotropic specimens. *Composites Science and Technology* 2008;68:80–9.
- [14] Sun XC, Wisnom MR, Hallett SR. Interaction of inter- and intralaminar damage in scaled quasi-static indentation tests: Part 2 - Numerical simulation. *Composite Structures* 2016;136:727–42.

- [15] Bouvet C, Castanié B, Bizeul M, Barrau J-J. Low velocity impact modelling in laminate composite panels with discrete interface elements. *International Journal of Solids and Structures* 2009;46:2809–21.
- [16] Bouvet C, Rivallant S, Barrau JJ. Low velocity impact modeling in composite laminates capturing permanent indentation. *Composites Science and Technology* 2012;72:1977–88.
- [17] Hongkarnjanakul N, Bouvet C, Rivallant S. Validation of low velocity impact modelling on different stacking sequences of CFRP laminates and influence of fibre failure. *Composite Structures* 2013;106:549–59.
- [18] Aymerich F, Dore F, Priolo P. Prediction of impact-induced delamination in cross-ply composite laminates using cohesive interface elements. *Composites Science and Technology* 2008;68:2383–90.
- [19] de Moura MFS., Gonçalves JP. Modelling the interaction between matrix cracking and delamination in carbon–epoxy laminates under low velocity impact. *Composites Science and Technology* 2004;64:1021–7.
- [20] Zhang Y, Zhu P, Lai X. Finite element analysis of low-velocity impact damage in composite laminated plates. *Materials & Design* 2006;27:513–9.
- [21] Abisset E, Daghia F, Sun XC, Wisnom MR, Hallett SR. Interaction of inter- and intralaminar damage in scaled quasi-static indentation tests: Part 1 – Experiments. *Composite Structures* 2016;136:712–26.
- [22] Riccio A, De Luca A, Di Felice G, Caputo F. Modelling the simulation of impact induced damage onset and evolution in composites. *Composites Part B: Engineering* 2014;66:340–7.
- [23] Riccio A, Di Felice G, LaManna G, Antonucci E, Caputo F, Lopresto V, et al. A Global–Local Numerical Model for the Prediction of Impact Induced Damage in Composite Laminates. *Applied Composite Materials* 2014;21:457–66.
- [24] F. Caputo, Lamanna G, Luca A De, Borrelli R, Franchitti S. Global-Local FE Simulation of a Plate LVI Test. *Structural Durability & Health Monitoring* 2013;9:253–67.
- [25] Caputo F, De Luca A, Lamanna G, Lopresto V, Riccio A. Numerical investigation of onset and evolution of LVI damages in Carbon–Epoxy plates. *Composites Part B: Engineering* 2015;68:385–91.
- [26] Riccio A, Ricchiuto R, Damiano M, Scaramuzzino F. A Numerical Study on the Impact Behaviour of an All-composite Wing-box. *Procedia Engineering* 2014;88:54–61.
- [27] Gigliotti L, Pinho ST. Multiple length/time-scale simulation of localized damage in composite structures using a Mesh Superposition Technique. *Composite Structures* 2014.
- [28] Sellitto A, Borrelli R, Caputo F, Riccio A, Scaramuzzino F. Methodological approaches for kinematic coupling of non-matching finite element meshes. *Procedia Engineering* 2011;10:421–6.
- [29] Sellitto A, Borrelli R, Caputo F, Riccio A, Scaramuzzino F. Application to plate components of a kinematic global-local approach for non-matching finite element meshes. *International Journal of Structural Integrity* 2012;3:260–73.
- [30] Ledentsov D, Düster A, Volk W, Wagner M, Heinle I, Rank E. Model adaptivity for industrial application of sheet metal forming simulation. *Finite Elements in Analysis and Design* 2010;46:585–600.
- [31] Krueger R, Ratcliffe JG, Minguet PJ. Panel stiffener debonding analysis using a shell/3D modeling technique. *Composites Science and Technology* 2009;69:2352–62.

- 745 [32] Krueger R, Minguet PJ. Analysis of composite skin–stiffener debond specimens using a
746 shell/3D modeling technique. *Composite Structures* 2007;81:41–59.
- 747 [33] Krueger R, Paris IL, Kevin O’Brien T, Minguet PJ. Comparison of 2D finite element modeling
748 assumptions with results from 3D analysis for composite skin-stiffener debonding. *Composite*
749 *Structures* 2002;57:161–8.
- 750 [34] Krueger R, O’Brien T. A shell/3D modeling technique for the analysis of delaminated
751 composite laminates. *Composites Part A: Applied Science and Manufacturing* 2001;32:25–44.
- 752 [35] Cho M, Kim J-S. Bifurcation Buckling Analysis of Delaminated Composites Using Global-
753 Local Approach. *AIAA Journal* 1997;35:1673–6.
- 754 [36] Davila CG, Johnson ER. Analysis of Delamination Initiation in Postbuckled Dropped-Ply
755 Laminates. *AIAA Journal* 1993;31:721–7.
- 756 [37] Harper PW, Hallett SR. Cohesive zone length in numerical simulations of composite
757 delamination. *Engineering Fracture Mechanics* 2008;75:4774–92.
- 758 [38] Czabaj MW, Ratcliffe JG. Comparison of intralaminar and interlaminar mode I fracture
759 toughnesses of a unidirectional IM7/8552 carbon/epoxy composite. *Composites Science and*
760 *Technology* 2013;89:15–23.
- 761 [39] Pinho ST, Robinson P, Iannucci L. Developing a four point bend specimen to measure the mode
762 I intralaminar fracture toughness of unidirectional laminated composites. *Composites Science*
763 *and Technology* 2009;69:1303–9.
- 764 [40] Ramesh R, Kishore, Rao RMVGK. Dry wear studies on glass-fibre-reinforced epoxy
765 composites. *Wear* 1983;89:131–6.
- 766 [41] ASTM standard D7136 / D7136M. Standard Test Method for Measuring the Damage
767 Resistance of a Fiber-Reinforced Polymer Matrix Composite to a Drop-Weight Impact Event
768 2003.
- 769 [42] Hallett SR, Green BG, Jiang WG, Wisnom MR. An experimental and numerical investigation
770 into the damage mechanisms in notched composites. *Composites Part A: Applied Science and*
771 *Manufacturing* 2009;40:613–24.
- 772 [43] O’Brien T, Johnston W, Toland G. Mode II interlaminar fracture toughness and fatigue
773 characterization of a graphite epoxy composite material. NASA Langley Research Center;
774 Hampton, VA, United States: 2010.
- 775 [44] Suemasu H, Majima O. Multiple Delaminations and their Severity in Circular Axisymmetric
776 Plates Subjected to Transverse Loading. *Journal of Composite Materials* 1996;30:441–53.
- 777 [45] Suemasu H, Wisnom MR, Sun XC, Hallett SR. An analytical study on multiple delaminations
778 and instability in nonlinear plate subjected to transverse concentrated load. 13th Japan
779 International SAMPE Symposium and Exhibition 2013.
- 780 [46] Olsson R. Mass criterion for wave controlled impact response of composite plates. *Composites*
781 *Part A: Applied Science and Manufacturing* 2000;31:879–87.
- 782 [47] Suemasu H, Majima O. Multiple Delaminations and their Severity in Nonlinear Circular Plates
783 Subjected to Concentrated Loading. *Journal of Composite Materials* 1998;32:123–40.
- 784 [48] Abrate S. Impact on composite structures. Cambridge University Press; 2005.
- 785 [49] González EV, Maimí P, Camanho PP, Lopes CS, Blanco N. Effects of ply clustering in
786 laminated composite plates under low-velocity impact loading. *Composites Science and*
787 *Technology* 2011;71:805–17.

788 [50] Schoeppner GA, Abrate S. Delamination threshold loads for low velocity impact on composite
789 laminates. *Composites Part A: Applied Science and Manufacturing* 2000;31:903–15.

790 [51] Lopes CS, Seresta O, Coquet Y, Gürdal Z, Camanho PP, Thuis B. Low-velocity impact damage
791 on dispersed stacking sequence laminates. Part I: Experiments. *Composites Science and*
792 *Technology* 2009;69:926–36.

793 [52] Fuoss E, Straznicky P, Poon C. Effects of stacking sequence on the impact resistance in
794 composite laminates—Part 1: parametric study. *Composite Structures* 1998;8223.

795 [53] Liu H. Ply clustering effect on composite laminates under low-velocity impact using FEA.
796 Cranfield University, School of Engineering, 2012.

797 [54] Nettles A, Douglas M, Estes E. Scaling effects in carbon/epoxy laminates under transverse
798 quasi-static loading. NASA Technical Report 1999;NASA/TM-19.

799 [55] Davies GAO, Zhang X. Impact damage prediction in carbon composite structures. *International*
800 *Journal of Impact Engineering* 1995;16:149–70.

801 [56] Davies GAO, Robinson P, Robson J, Eady D. Shear driven delamination propagation in two
802 dimensions. *Composites Part A: Applied Science and Manufacturing* 1997;28:757–65.

803 [57] Greenhalgh E, Meeks C, Clarke A, Thatcher J. The effect of defects on the performance of post-
804 buckled CFRP stringer-stiffened panels. *Composites Part A: Applied Science and*
805 *Manufacturing* 20031;34:623–33.

806 [58] Jose S, Ramesh Kumar R, Jana MK, Venkateswara Rao G. Intralaminar fracture toughness of
807 a cross-ply laminate and its constituent sub-laminates. *Composites Science and Technology*
808 2001;61:1115–22.

809